Photonics-Based Multidomain Features Extraction for Radio Frequency Signals

Jiewen Ding, *Student Member, IEEE*, Dan Zhu, *Member, IEEE*, Yue Yang, *Student Member, IEEE*, Zhouyang Pan, *Student Member, IEEE*, and Shilong Pan, *Fellow, IEEE*

***Abstract*— A photonics-based multidomain features extraction approach for radio frequency (RF) signals is proposed and demonstrated. Through the time-mapped Fourier transform (TM-FT) and optical interference on the RF signals captured by multiple antennas, the spectrum and the 2-D angle of arrival (AOA) of the RF signals are mapped to the time domain simultaneously. Thus, the simultaneous multidomain features extraction of the RF signals will be guaranteed. In addition, due to the use of the chirped optical pulse with MHz repetition rate as the time window for the features extraction, the proposed scheme can analyze wideband and transient RF signals. In the experiment, the multidomain features of 4-GHz wideband RF signals and 5-ns RF transient signals are extracted, and the signal types are classified successfully. The frequency measurement range of 6–16 GHz with an error of ±25 MHz and the 2-D AOA measurement range of ±40° with an error of ±2.5° are verified. The proposed approach provides an innovative option for real-time multidomain features extraction and classification of RF signals in complex electromagnetic environments.**

***Index Terms*— Feature extraction, frequency-to-time mapping (FTM), microwave photonics, signal classification, spectrum analysis.**

I. Introduction

RADIO frequency (RF) signal features extraction is a key technology for electromagnetic environment perception, which has wide applications in the radio astronomy, cognitive radar, and intelligent wireless communication systems [1], [2], [3]. In general, the features of RF signals can be categorized into four domains: the time domain, the spatial domain, the frequency domain, and others [4], as shown in Fig. 1. In practical scenarios, RF signals are usually nonstationary in the time domain and nonuniform in the spatial domain. Therefore, to dynamically extract RF signal features, the joint analyses of features in multidomain are usually performed, such as short time Fourier transform (STFT) [6], fractional Fourier transform (FrFT) [7], wavelet transform (WT) [8], and multisignals classification (MUSIC) algorithm [9]. However, these methods depend on high-performance digital signal processing (DSP) engines [10] to execute complex digital computations. With the rapid increasing of the frequency, bandwidth, and modulation rate of the RF signals, it becomes a challenge for the traditional DSP-based methods to achieve real-time, wideband, and high-precision feature extraction simultaneously.

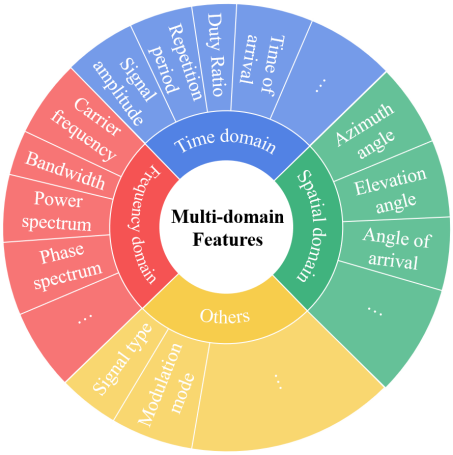

Fig. 1. Features of RF signals in multidomain.

Photonics-based RF signal features extraction is considered as a potential solution to overcome this challenge due to the wideband processing, low transmission loss, and anti-electromagnetic interference advantages brought by photonics [11], [12], [13]. Several photonics-based joint time–frequency feature extraction schemes for RF signals have been proposed [17], [18], [19], [20], [21], [22], [23], [24], [25], [26], [27]. The basic principle is to achieve the real-time frequency-to-time mapping (FTM) of the RF signals in the optical domain by using the dispersive medium [14], [15]. An all-optical STFT was proposed in [17]. The windowing and FTM of the RF signals modulated on the chirped optical pulses are realized simultaneously by cascading linear chirped fiber Bragg gratings (LCFBGs) with different center wavelengths. Similarly, an all-optical WT was achieved using LCFBG arrays with different bandwidths [18]. However, suffering from the limitation of dispersion values [19], the frequency resolution is larger than 1 GHz. In [20], a bandwidth-magnified STFT is proposed to improve frequency resolution. This scheme

Manuscript received 13 August 2023; revised 4 October 2023; accepted 10 October 2023. Date of publication 26 October 2023; date of current version 5 June 2024. This work was supported in part by the National Natural Science Foundation of China under Grant 61971222 and Grant 62271249 and in part by the Natural Science Foundation of Jiangsu Province under Grant BK20220076. *(Corresponding authors: Dan Zhu; Shilong Pan.)*

The authors are with the National Key Laboratory of Microwave Photonics, College of Electronic and Information Engineering, Nanjing University of Aeronautics and Astronautics, Nanjing 210016, China (e-mail: dingjw@nuaa.edu.cn; danzhu@nuaa.edu.cn; yangyue96@nuaa.edu.cn; Pan_zy@nuaa.edu.cn; pans@nuaa.edu.cn).

Color versions of one or more figures in this article are available at https://doi.org/10.1109/TMTT.2023.3325040.

Digital Object Identifier 10.1109/TMTT.2023.3325040

0018-9480 © 2023 IEEE. Personal use is permitted, but republication/redistribution requires IEEE permission.
See https://www.ieee.org/publications/rights/index.html for more information.

Authorized licensed use limited to: NANJING UNIVERSITY OF AERONAUTICS AND ASTRONAUTICS. Downloaded on October 18,2024 at 07:22:27 UTC from IEEE Xplore. Restrictions apply.

disperses and magnifies the spectrum of RF signal through the optical vernier effect [21] and then performs FTM on the bandwidth-magnified RF signal. The frequency resolution of 60 MHz is experimentally verified [22], [23]. A universal approach for real-time gap-free spectral analysis of nonstationary signal is reported in [24], [25], [26], and [27]. Through a combination of optical sampling of the RF signal followed by linear dispersive propagation, dynamic Fourier analysis of the RF signal is achieved without windowing. Nanosecond time resolution and FTM speed are verified.

To analyze the distribution of RF spectrum in the spatial domain, photonics-based simultaneous extraction schemes of RF features in the frequency and spatial domains are investigated. A photonic-based k-space tomography of RF signals is presented in [29], [30], and [31]. The spatial spectrum of RF signals can be reconstructed through the temporal aperture composed of random fibers compact and the lens-based optics. However, this scheme offers limited extraction speed, constrained by the refresh rate of CCD (typically in the kilohertz range) and the use of complex reconstruction algorithms. In [32] and [33], a photonics-based simultaneous angle-of-arrival (AOA) and frequency measurement system is proposed. The wideband RF signal is downconverted to intermediate frequency (IF) by a frequency-stepped local oscillation (LO) through an in-phase and quadrature (I/Q) downconversion [34], [35]. The features of RF signals in the frequency and spatial domains are extracted by array signal processing [36]. Nevertheless, the long sweep time of the scheme makes it unsuitable for nonstationary signals. In summary, the existing photonics-based RF feature extraction schemes are difficult to achieve real-time feature extraction in time, frequency, and spatial domains simultaneously.

In this article, a photonics-based multidomain features extraction scheme for RF signals has been proposed and demonstrated. The proposed approach implements a simultaneous mapping of the spectrum and AOA of the RF signals to the time domain, guaranteeing the extraction of the multidomain features simultaneously without computationally intensive algorithms. This is achieved through simultaneously performing the time-mapped Fourier transform (TM-FT) and the optical interference on the RF signals captured by multiple antennas and modulated on a dual-polarization dual-parallel Mach–Zehnder modulator (DP-DPMZM). Since a single-shot TM-FT can be completed in one period of the optical pulses with MHz repetition rate, the real-time joint time–frequency analysis of the wideband and transient RF signals can be achieved by the proposed scheme. In addition, different from the classical approaches that extract the 1-D AOA [12], [37], the implementation of polarization-multiplexed electro-optical modulation extends the spatial feature extraction to 2-D AOA (azimuth and elevation angles) without increasing the complexity of the system. An experimental setup is established and demonstrated. The time, frequency, and spatial multidomain joint features of 4-GHz wideband signals and transient signals with a 5-ns duration are successfully extracted. The frequency measurement range of 6–16 GHz with an error of ±25 MHz and the 2-D AOA range of ±40° with an error of ±2.5° are experimentally demonstrated. Furthermore, based on the joint time–frequency features or the time-mapped spectrogram (TM-SP), the RF signals are automatically classified by a one-stage detection algorithm successfully.

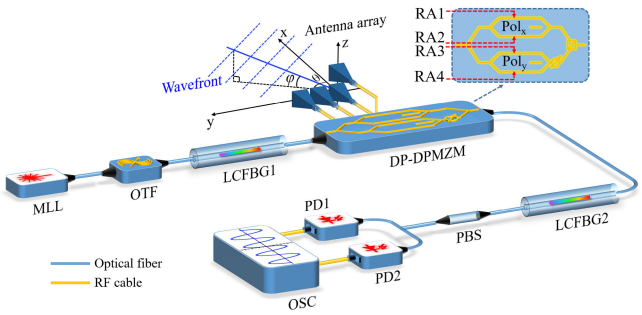

Fig. 2. Schematic of the proposed multidomain RF signal features extraction scheme. MLL: mode-lock laser. OTF: optical tunable filter. LCFBG: linear chirped fiber Bragg grating. DP-DPMZM: dual-polarization dual-parallel Mach–Zehnder modulator. RA: receive antenna. PBS: polarization beam splitter. PD: photodetector. OSC: oscilloscope.

II. Principle

The schematic of the proposed multidomain RF signal feature extraction scheme is shown in Fig. 2. The Gaussian optical pulses are generated by a mode-locked laser (MLL), which are then shaped by an optical tunable filter (OTF) and used as the optical carrier. The envelope of the optical pulse can be mathematically expressed as follows:

$$E_1(t) = A\exp\left(-\frac{t^2}{2T_0^2}\right) \tag{1}$$

where A is the amplitude of the optical pulse, and T_0 is the full-width at half-maximum (FWHM) of the optical pulse. The optical pulse is time-stretched through LCFBG1 with a second dispersion value of $\beta_2 z$. The temporal waveform output from LCFBG1 is as follows:

$$E_2(t) = \frac{A}{\left[1+\left(\frac{z}{L_D}\right)^2\right]^{1/4}}\exp\left\{-\frac{t^2}{2T_0^2\left[1+\left(\frac{z}{L_D}\right)^2\right]}\right\} \cdot\exp\left\{j\left[-\frac{\mathrm{sgn}(\beta_2)\frac{z}{L_D}}{2T_0^2\left[1+\left(\frac{z}{L_D}\right)^2\right]}t^2 + \frac{1}{2}\arctan\left(\mathrm{sgn}(\beta_2)\frac{z}{L_D}\right)\right]\right\} \tag{2}$$

where $L_D = T_0^2/|\beta_2|$. It can be seen that the FWHM of the time-stretched optical pulse is $T_1 = T_0[1+(z/L_D)^2]^{1/2}$, which can be regarded as the time window of the Fourier transform. The greater the second dispersion, the broader the time window, resulting in improved frequency resolution. Fig. 3 depicts the relative position of the antenna array to the far-field RF source in a Cartesian coordinate system. To avoid ambiguous phase differences or grating lobes [38], the spacing of adjacent antenna array elements $d_{RA} = c/2f_{max}$, where c is

Authorized licensed use limited to: NANJING UNIVERSITY OF AERONAUTICS AND ASTRONAUTICS. Downloaded on October 18,2024 at 07:22:27 UTC from IEEE Xplore. Restrictions apply.

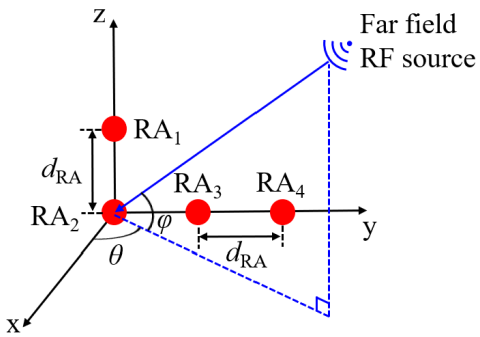

Fig. 3. Schematic of the relative positions of the far-field RF source and the antenna array.

the velocity of electromagnetic waves in vacuum and $f_{\max}$ is the maximum working frequency of the antenna array. The RF signals received by the four receive antennas (RAs) can be expressed as follows:

$$s_n(t) = V_{\mathrm{RF}} \cos(\omega_{\mathrm{RF}} t + \phi_n) n \in [1, 2, 3, 4] \tag{3}$$

where V_{RF} is the amplitude of the RF signal, ω_{RF} is the angular frequency of the RF signal, and ϕ_n is the phase of the RF signal received by RA_n.

Based on the RF source orientation shown in Fig. 3, the phase ϕ_n can be expressed as follows:

$$\begin{bmatrix} \phi_1 \\ \phi_2 \\ \phi_3 \\ \phi_4 \end{bmatrix} = \frac{\omega_{\mathrm{RF}}}{c} \cdot \begin{bmatrix} 0 & 0 & d_{\mathrm{RA}} \\ 0 & 0 & 0 \\ 0 & d_{\mathrm{RA}} & 0 \\ 0 & 2d_{\mathrm{RA}} & 0 \end{bmatrix} \cdot \begin{bmatrix} \cos(\theta)\cos(\varphi) \\ \sin(\theta)\cos(\varphi) \\ \sin(\varphi) \end{bmatrix} \tag{4}$$

where θ and φ are the azimuth and elevation angles of the RF signal, respectively. As can be seen, there are phase differences in the RF signals received by four RAs, which can be used to extract the spatial domain features.

The RF signals are modulated to the time-stretched optical pulse by a DP-DPMZM. The DP-DPMZM is composed of two polarization-orthogonal DPMZM (Pol_x-DPMZM and Pol_y-DPMZM). The RF signals received by RA_1 and RA_2 and the RF signals received by RA_3 and RA_4 are modulated to the time-stretched optical pulse $E_2(t)$ by the Pol_x-DPMZM and the Pol_y-DPMZM, respectively. The received RF signals are modulated to the time-stretched optical pulse $E_2(t)$, and the optical signal output from the DP-DPMZM is as follows:

$$\begin{aligned} &E_3(t) \\ &= \hat{e_x} E_2(t) \frac{J_1(\beta)}{2} \gamma \\ &\quad \left\{ \left[\exp(j\omega_{\mathrm{RF}} t + j\phi_1) + \exp(-j\omega_{\mathrm{RF}} t - j\phi_1) \right] \right. \\ &\quad \left. + \left[\exp(j\omega_{\mathrm{RF}} t + j\phi_2) + \exp(-j\omega_{\mathrm{RF}} t - j\phi_2) \right] \exp(j\psi) \right\} \\ &\quad + \hat{e_y} E_2(t) \frac{J_1(\beta)}{2} \gamma \\ &\quad \left\{ \left[\exp(j\omega_{\mathrm{RF}} t + j\phi_4) + \exp(-j\omega_{\mathrm{RF}} t - j\phi_4) \right] \right. \\ &\quad \left. + \left[\exp(j\omega_{\mathrm{RF}} t + j\phi_3) + \exp(-j\omega_{\mathrm{RF}} t - j\phi_3) \right] \exp(j\psi) \right\} \end{aligned} \tag{5}$$

where $\hat{e_x}$ and $\hat{e_y}$ are the two orthogonal unit vectors, which denote the two orthogonal polarization states. In addition, $J_1(\cdot)$ is the first Bessel function, and γ, V_π, and ψ are the, the insertion loss, the half-wave voltage, and the additional phase introduced by the bias voltage of the DP-DPMZM, respectively. $\beta = \pi V_{\mathrm{RF}}/V_\pi$ represents the modulation depth. Both DPMZMs in the DP-DPMZM work at the orthogonal bias point, and the sub-MZMs in two DPMZMs work at the minimum bias point. The modulated optical signal is then input to LCFBG2 with a second dispersion value of $-\beta_2 z$, to realize the frequency-to-time and AOA-to-amplitude ratio mapping. The two polarization-orthogonal optical signals are separated by a polarization beam splitter and then injected into two photodetectors (PDs): PD1 and PD2, whose output are as follows:

$$\begin{cases} I_1(t) = \dfrac{\eta_1 \gamma^2 J_1(\beta)^2}{2} \\ \quad \cdot \left\{ \exp\left[-\dfrac{(t - \omega_{\mathrm{RF}}\beta_2 z)^2}{T_0^2} \right] [1 + \cos(\phi_2 - \phi_1 + \psi)] \right. \\ \quad \left. + \exp\left[-\dfrac{(t + \omega_{\mathrm{RF}}\beta_2 z)^2}{T_0^2} \right] [1 + \cos(\phi_2 - \phi_1 - \psi)] \right\} \\ I_2(t) = \dfrac{\eta_2 \gamma^2 J_1(\beta)^2}{2} \\ \quad \cdot \left\{ \exp\left[-\dfrac{(t - \omega_{\mathrm{RF}}\beta_2 z)^2}{T_0^2} \right] [1 + \cos(\phi_3 - \phi_4 + \psi)] \right. \\ \quad \left. + \exp\left[-\dfrac{(t + \omega_{\mathrm{RF}}\beta_2 z)^2}{T_0^2} \right] [1 + \cos(\phi_3 - \phi_4 - \psi)] \right\} \end{cases} \tag{6}$$

where η_1 and η_2 denote the responsiveness of PD1 and PD2, respectively. It can be seen that the temporal waveforms' output from PD1 and PD2 exhibits two satellite pulses each, with a time interval linearly correlated to ω_{RF}, respectively. These two satellite pulses can be interpreted as the TM-FT of the received RF signal at positive and negative frequencies, respectively. The frequency of the RF signal can be expressed as follows:

$$f_{\mathrm{RF}} = \frac{\Delta t}{4\pi\beta_2 z} \tag{7}$$

where Δt is the time interval of the two satellite pulses. As illustrated in Fig. 4(c) and (d), a 1-D array containing the Fourier transform of the RF signal at different times can be acquired through sampling the waveforms output from PD via an ADC for multiple periods equal to the repetition periods of the MLL. The original 1-D array is reshaped into a 2-D matrix, which presents the TM-SP of the RF signal.

Moreover, it can be seen from (6) and Fig. 4(c) that the amplitudes of the two satellite pulses are not uniform due to the optical interference. The amplitudes of the satellite pulses at PD1 and PD2 outputs are related to the phases of the RF signals received by RA_1, RA_2, RA_3, and RA_4, respectively, which can be used to extract the elevation angle and azimuth angle. Based on (4) and (6), four amplitude functions can be

Authorized licensed use limited to: NANJING UNIVERSITY OF AERONAUTICS AND ASTRONAUTICS. Downloaded on October 18,2024 at 07:22:27 UTC from IEEE Xplore. Restrictions apply.

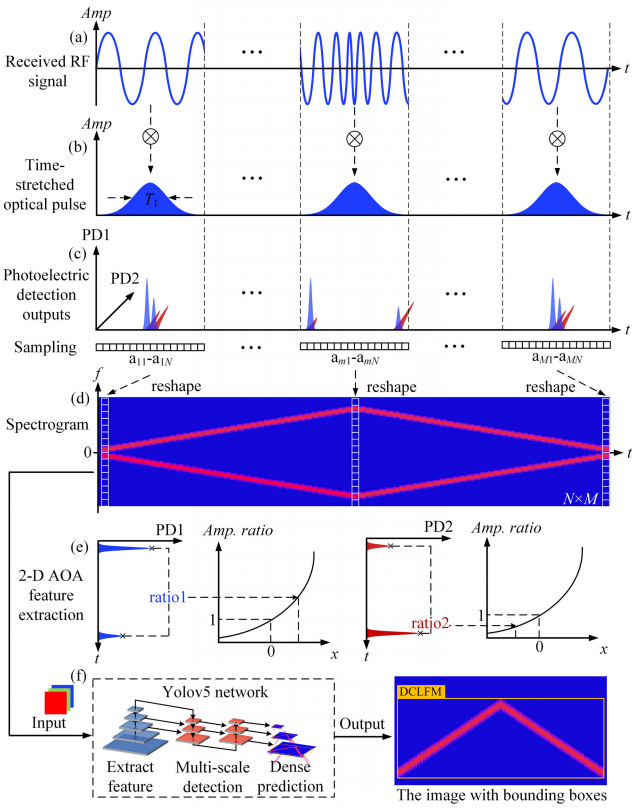

Fig. 4. Basic principle of the proposed photonics-based multidomain feature extraction method. The temporal waveforms of (a) received RF signal (taking a dual-chirp LFM signal as an example), (b) time-stretched optical pulses, and (c) outputs of PD1 (blue) and PD2 (red). (d) TM-SP of the received RF signal generated by reshaping the 1-D array. Schematic of (e) 2-D AOA feature extraction and (f) signal classification.

expressed as follows:

$$\begin{cases} A_1 = \dfrac{\eta_2\gamma^2}{2} J_1\left(\dfrac{\pi V_{\mathrm{RF}}}{V_\pi}\right)^2 \left\{1+\cos\left[\dfrac{\pi f_{\mathrm{RF}}}{f_{\max}}\sin(\varphi)+\psi\right]\right\} \\ A_2 = \dfrac{\eta_2\gamma^2}{2} J_1\left(\dfrac{\pi V_{\mathrm{RF}}}{V_\pi}\right)^2 \left\{1+\cos\left[\dfrac{\pi f_{\mathrm{RF}}}{f_{\max}}\sin(\varphi)-\psi\right]\right\} \\ A_3 = \dfrac{\eta_2\gamma^2}{2} J_1\left(\dfrac{\pi V_{\mathrm{RF}}}{V_\pi}\right)^2 \left\{1+\cos\left[\dfrac{\pi f_{\mathrm{RF}}}{f_{\max}}\sin(\theta)\cos(\varphi)+\psi\right]\right\} \\ A_4 = \dfrac{\eta_2\gamma^2}{2} J_1\left(\dfrac{\pi V_{\mathrm{RF}}}{V_\pi}\right)^2 \left\{1+\cos\left[\dfrac{\pi f_{\mathrm{RF}}}{f_{\max}}\sin(\theta)\cos(\varphi)-\psi\right]\right\} \end{cases} \tag{8}$$

where A_1 and A_2 denote the amplitudes of the two satellite pulses output from PD1, and A_3 and A_4 denote the amplitudes of the two satellite pulses output from PD2, respectively. As can be seen, the variables of the amplitude functions are related to not only the azimuth and elevation angles (θ and φ) but also the RF signal amplitude (V_{RF}). This indicates that there is ambiguity in the 2-D AOA measurement when the RF signal amplitude is unknown or time-variant. Therefore, to eliminate the ambiguity introduced by the RF signal amplitude, the proposed system measures the 2-D AOA by constructing the amplitude ratio function, which are expressed as follows:

$$F(x) = \frac{1+\cos\left[\frac{\pi f_{\mathrm{RF}}}{f_{\max}}\sin(x)-\psi\right]}{1+\cos\left[\frac{\pi f_{\mathrm{RF}}}{f_{\max}}\sin(x)+\psi\right]} \tag{9}$$

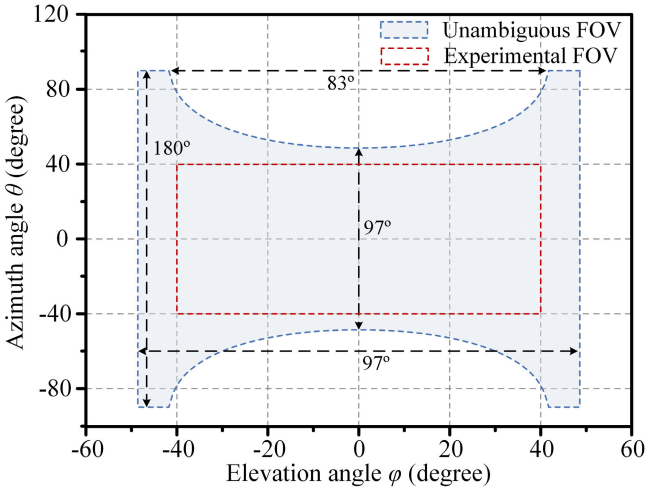

Fig. 5. Simulated 2-D FOV without ambiguity (blue dashed zone) and the 2-D FOV (red dashed zone) set in the experiments.

where $x = \varphi$ when measuring the elevation angles and $x = \sin^{-1}[\sin(\theta)\cos(\varphi)]$ when measuring the azimuth angles. It should be noted that based on the same amplitude ratio function, both the elevation and azimuth angles can be obtained.

To ensure that the amplitude ratio function shown in (9) has a unique constant solution, boundary conditions $-1 \le f_{\mathrm{RF}}\sin(x)/f_{\max} - \psi/\pi$ and $f_{\mathrm{RF}}\sin(x)/f_{\max} + \psi/\pi \le 1$ must be satisfied. In addition, when f_{RF} is set to $f_{\max}$, the range of x is minimized. Mathematically, it can be expressed as

$$\begin{cases} \sin^{-1}\left(-1+\dfrac{\psi}{\pi}\right) < \varphi < \sin^{-1}\left(1-\dfrac{\psi}{\pi}\right) \\ \sin^{-1}\left[\dfrac{-\pi+\psi}{\pi\cos(\varphi)}\right] < \theta < \sin^{-1}\left[\dfrac{\pi-\psi}{\pi\cos(\varphi)}\right]. \end{cases} \tag{10}$$

Since both the sub-DPMZMs in the DP-DPMZM work at the orthogonal biasing point, the additional phase ψ is known to be $\pi/4$. Based on (10), the simulated results of the unambiguous 2-D field-of-view (FOV) are depicted in the blue zone in Fig. 5, which takes on an H-shape due to the constraint of the boundary conditions. Since the amplitude ratio function at the FOV boundary is close to zero or infinity, resulting in an unacceptable 2-D AOA measurement error, the FOV is set to be $\pm 40°$ in the experiments as indicated by the red dashed zone in Fig. 5. After specifying the 2-D FOV, an amplitude ratio curve can be constructed by (9). As shown in Fig. 4(e), based on the amplitude ratio of the two satellite pulses and the constructed amplitude ratio curve, the elevation and azimuth angles can be acquired, respectively.

Besides the features extracted in the time, frequency, and spatial domains, the signal types can be automatically classified from the TM-SP by the you only look once (YOLOv5) neural network [39], which is pretrained and tested using some experimentally obtained TM-SP. As shown in Fig. 4(f), an image with bounding boxes and modulation types will be output, after image feature extraction, multiscale detection, and dense prediction. In this way, the proposed scheme successfully achieves the multidomain feature extraction and signal classification of the RF signals.

Authorized licensed use limited to: NANJING UNIVERSITY OF AERONAUTICS AND ASTRONAUTICS. Downloaded on October 18,2024 at 07:22:27 UTC from IEEE Xplore. Restrictions apply.

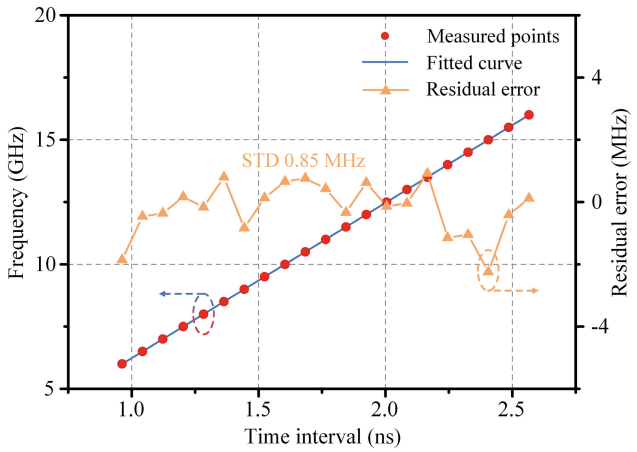

Fig. 6. FTM curve (blue curve) fitted by the experimental measured points and the residual error between the measured point and the fitted curve (yellow curve).

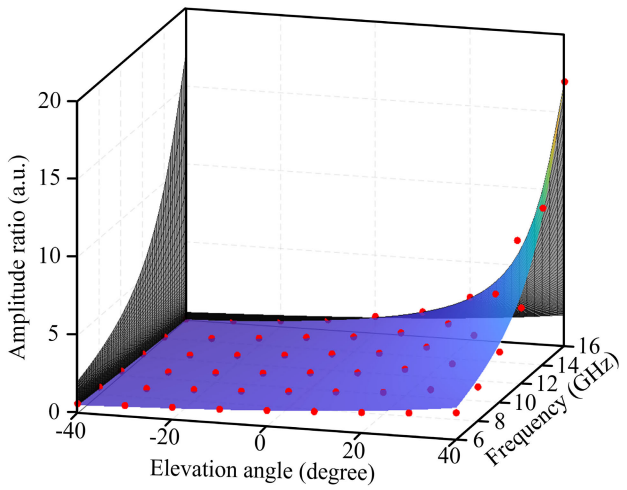

Fig. 7. Experimentally measured amplitude ratios (red dots) of the satellite pulses in the output FTM waveforms versus the frequencies and elevation angles of the received RF signals, and the fitted surface with 2-D projections.

III. Experiments and Results

A proof-of-concept experiment is taken based on the schematic in Fig. 2. An MLL (MenloSystems ELMO-780) is used to generate optical pulses with a repetition frequency of 100 MHz and an FWHM of 150 fs. The second dispersion values of LCFBG1 and LCFBG2 are ±10 ns/nm, respectively, and the working wavelengths for both are 1550–1555 nm. The OTF (Santec OTF-980) to shape the optical pulses has a 1-nm bandwidth and a 1552-nm center wavelength. A DP-DPMZM (Fujitsu FTM7977HQA) with a 3.5-V half-wave voltage and a 40-GHz bandwidth is used to modulate the received RF signals. Two PDs (Finisar VPDV3120R) with a 50-GHz bandwidth and a 0.6-A/W responsivity are used. The RF signals are generated by an arbitrary waveform generator (AWG, Keysight M8195A) with a 65-GSa/s sample rate. A real-time oscilloscope (OSC, DSO-X 92504A) with an 80-GSa/s sample rate is used to observe the output temporal waveforms.

A. Measurement of Multidomain Feature Mapping

To extract the multidomain features of the RF signals, the FTM curve and the amplitude ratio surface are experimentally measured, respectively. First, single-tone RF signals within the frequency range of 6–16 GHz are applied in the proposed system with a frequency step of 0.5 GHz. Through measuring the time intervals of the satellite pulses in the output FTM waveforms, the experimentally measured points are shown as the red dots in Fig. 6. The blue curve indicates the FTM curve by fitting the measured points. It can be seen that the frequency of the RF signal is proportional to the time interval of the satellite pulses, which is consistent with (7). It is worth noting that the slope of the fit FTM curve is approximately 6.25 GHz/ns, and considering the 10-ns period of the MLL, the maximum measurement bandwidth of the experimental system is calculated to be 62.5 GHz. The residual errors between the measured results and the fitted curve are represented by the yellow solid line in Fig. 6, with a standard deviation (STD) of 0.85 MHz within the frequency range of 6–16 GHz.

Second, four single-tone signals with phase differences generated from the AWG are used as the received RF signals with different 2-D AOAs. The four single-tone signals are injected to the four RF ports of the DP-DPMZM as the RF signals received by RA_1, RA_2, RA_3, and RA_4, respectively. The frequencies of the RF signals are tuned with a 2-GHz step within the frequency range of 6−16 GHz. The RF signals have the elevation angles from −40° to 40° with a step of 10° and the azimuth angle of 0°. In the experiment, the satellite pulses output from PD1 is observed by the OSC. The experimentally measured amplitude ratios are shown in red dots in Fig. 7, which are used to fit the amplitude ratio surface. It can be seen that the amplitude ratio exhibits a steeper growth when the elevation angles are larger. Theoretically, at the boundary of the unambiguous FOV in Fig. 5, the amplitude ratio converges to zero or infinity. In this case, the amplitude ratio offset introduced by the amplitude jitter of satellite pulses will cause inaccurate feature extraction. Therefore, to ensure high feature extraction accuracy, the experimental 2-D AOA range is set to ±40°. After extracting the RF signal frequency from the FTM curve, the amplitude ratio curves for the spatial feature extraction can be constructed from intersecting lines between the fitted surface and the definitive frequency plane. The back projection (the plane of elevation angle and amplitude ratio) in Fig. 7 is the set of all amplitude ratio curves in the measurement frequency range. Finally, the elevation angle of the RF signal is obtained from the measured satellite pulse amplitude ratio through the amplitude ratio curve, achieving the feature extraction of the frequency domain. It should be noted that the azimuth angle can also be indirectly measured by the amplitude ratio surface in Fig. 7 based on (9).

B. Extraction of Multidomain Features

To verify the performance of the multidomain features extraction, an up-chirped linear frequency-modulated (LFM) signal and a single-tone transient signal with a time duration of 5 ns generated by the AWG are used as the signal under

Authorized licensed use limited to: NANJING UNIVERSITY OF AERONAUTICS AND ASTRONAUTICS. Downloaded on October 18,2024 at 07:22:27 UTC from IEEE Xplore. Restrictions apply.

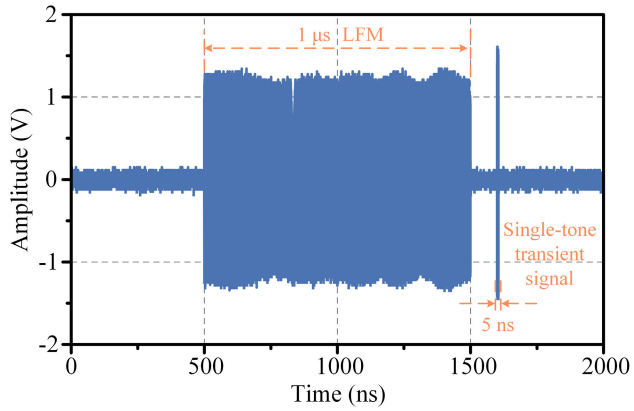

Fig. 8. Temporal waveform of the SUT, including a 1-μs up-chirped LFM signal and a 5-ns single-tone transient signal.

TABLE I
MULTIDOMAIN FEATURES OF THE SUT

	Up-chirped LFM signal	Single-tone transient signal
Duration (ns)	1000	5
Frequency (GHz)	12-16	6
Elevation angle (degree)	25.0	-30.0
Azimuth angle (degree)	-30.0	30.0

test (SUT). The temporal waveform of the SUT is shown in Fig. 8, and its multidomain features are defined in Table I.

Fig. 9(a) and (b) shows the output waveforms of PD1 and PD2, respectively. Intuitively, it can be seen that the SUT composed by two signals, one of which has a duration of 1 μs, and the other transient one has a duration of 5 ns. Furthermore, the insets in Fig. 9 provide two additional pieces of information regarding the SUT. First, by comparing the time intervals of the satellite pulses, it is evident that the frequency of the transient signal is significantly lower than that of the other signal. Second, the amplitude of the left satellite pulse is higher than that of the right pulse, indicating a positive amplitude ratio and, consequently, a positive AOA. Conversely, a negative amplitude ratio corresponds to a negative AOA. Therefore, based on Fig. 9(a), it can be concluded that the signal with a duration of 1 μs has a positive elevation angle but a negative azimuth angle. Similarly, the insets in Fig. 9(b) indicate a negative elevation angle but a positive azimuth angle for the transient signal.

Fig. 10 shows the TM-SP of the SUT generated by reshaping the data in Fig. 9(a) into a 2-D matrix. As can be seen that the spectra of an up-chirped LFM signal and a single-tone transient signal are observed successfully. The results in Figs. 9 and 10 confirm the capability of the proposed scheme to extract the time- and frequency-domain features of wideband and transient signals. It should be highlighted that the proposed system performs the optical Fourier transform of the SUT for 200 times within 2 μs, with the computational speed far beyond that of the current DSPs [40].

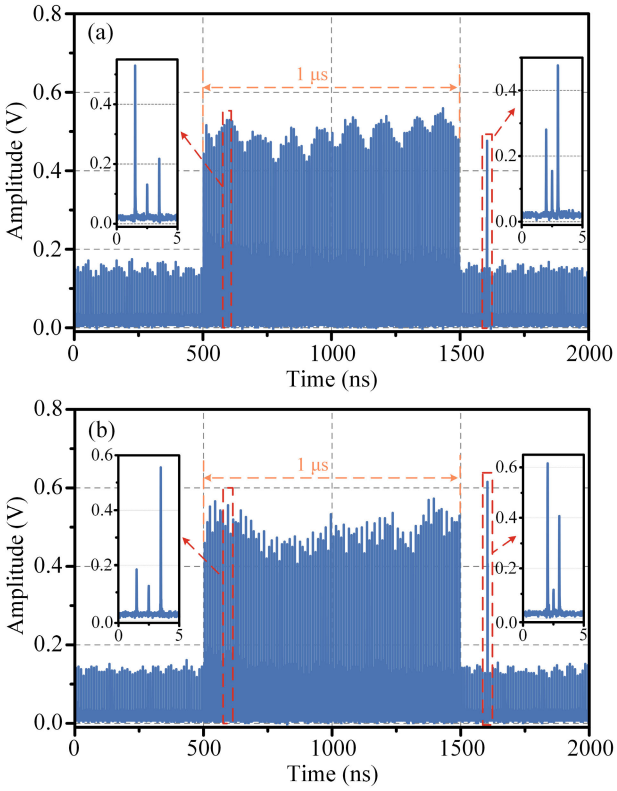

Fig. 9. Output temporal waveforms of (a) PD1 and (b) PD2. Inset: output temporal waveforms in detail at different time locations.

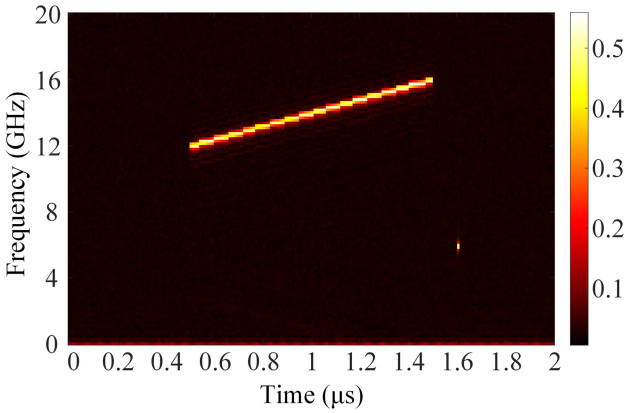

Fig. 10. Experimentally obtained TM-SP of the SUT by reshaping the 1-D array generated from PD1 into a 2-D matrix.

Based on the fitted FTM curve and the amplitude ratio surface, the frequencies, elevation, and azimuth angles of the SUT can be obtained from the output waveforms of PD1 and PD2. Fig. 11(a) shows the experimentally measured elevation angles and the frequency distribution of the SUT, and Fig. 11(b) shows the experimentally measured azimuth angles and the frequency distribution of the SUT. The top plots of Fig. 11(a) and (b) show the histogram of the SUT frequency distribution on the frequency axis, and the right plots show the histogram of the SUT elevation and azimuth angle distribution on the elevation and azimuth angle axes. As can be seen, the experimentally measured frequency of the transient single-tone signal is 6.0002 GHz, and the measured frequencies of the

Authorized licensed use limited to: NANJING UNIVERSITY OF AERONAUTICS AND ASTRONAUTICS. Downloaded on October 18,2024 at 07:22:27 UTC from IEEE Xplore. Restrictions apply.

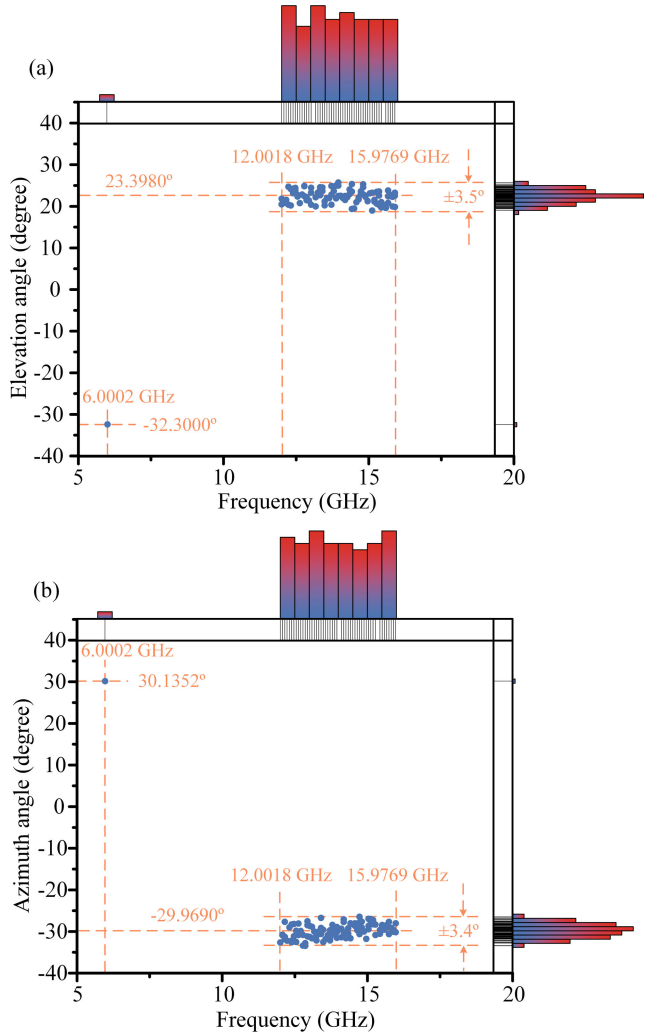

Fig. 11. Experimentally measured (a) elevation angles and (b) azimuth angles and the frequency distribution of the SUT.

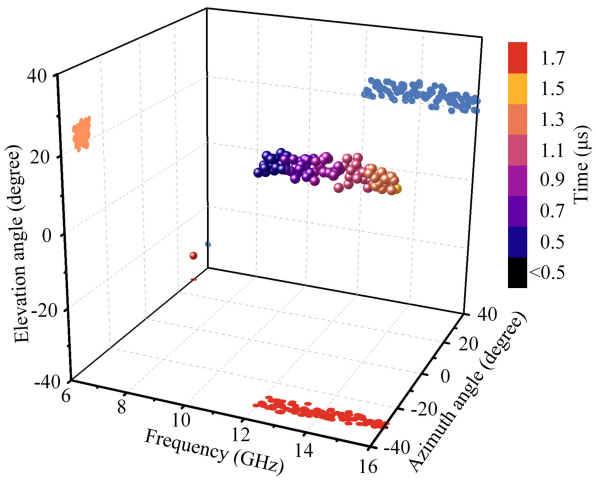

Fig. 12. Distribution of the features extracted of the SUT in the time, frequency, and spatial domains.

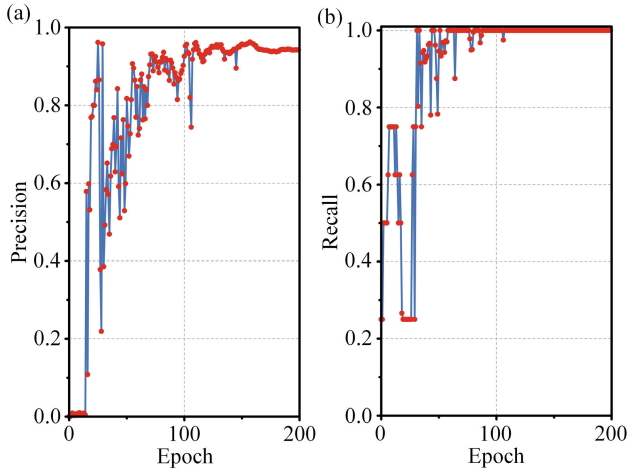

Fig. 13. (a) Precision and (b) recall of the neural network versus epochs during training.

up-chirped LFM signal are 12.0018−15.9769 GHz. The frequencies of the up-chirped LFM signal show an approximate uniform distribution along the frequency axis, which is consistent with the spectrogram. The measured 2-D AOAs of the transient signal are −32.3000° and 30.1352°. The angles of the up-chirped LFM signal show an approximate Gaussian distribution. Therefore, the average of the measured points in the 12−16 GHz range is used to represent the elevation and azimuth angles of the up-chirped LFM signal. It can be seen that the measured elevation angle of the up-chirped LFM signal is 23.3980° with an uncertainty of ±3.5°, and the measured azimuth angle is −29.9690° with an uncertainty of ±3.4°. In conclusion, the extracted frequencies, 2-D AOA of the SUT are in agreement with its actual values presented in Table I. Through a comparison between the predefined parameters and the measured results, the frequency error for both the transient RF signal and the wideband RF signal is within ±25 MHz, while the 2-D AOA error is within ±2.5°.

By conducting a joint analysis of the time–frequency feature extraction results presented in Fig. 10 and the feature extraction outcomes in the frequency and spatial domains depicted in Fig. 11, the extraction of multidomain features is accomplished, as illustrated in Fig. 12. The 3-D axes of Fig. 12 represent frequency, azimuth, and elevation angles, respectively, and the color map represents time. The red, blue, and yellow dots indicate the projection of the multidomain features of the SUT along the three axes, respectively. Therefore, the time-, frequency-, and spatial-domain features of the SUT are successfully extracted simultaneously, validating the simultaneous multidomain features extraction capability for RF signals of the proposed scheme.

C. RF Signal Classification

Then, the RF signals are classified by the YOLOv5 neural network. The 90 spectrograms were generated through the experimental system, among which 80 TM-SPs were used as the training sets, and the other ten TM-SPs were used as the verification sets. The used signal types include dual-chirped LFM signals, up-chirped LFM signals, down-chirped LFM signals, transient signals and continuous single-tone signals. Each TM-SP contains at least one signal type. The neural network is trained for 200 epochs on an NVDIA GeForce RTX2060 graphics card. Fig. 13(a) and (b), respectively,

Authorized licensed use limited to: NANJING UNIVERSITY OF AERONAUTICS AND ASTRONAUTICS. Downloaded on October 18,2024 at 07:22:27 UTC from IEEE Xplore. Restrictions apply.

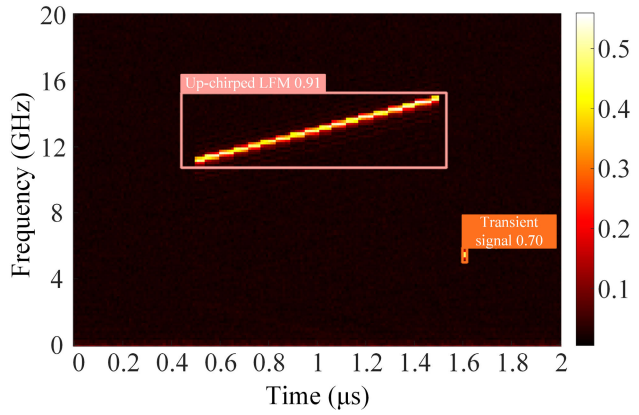

Fig. 14. Result of RF signal classification based on the TM-SP shown in Fig. 10.

shows the precision and recall of the neural network during training, which can be used to evaluate the training effect. The precision indicates the percentage of the all predictions that were predicted correctly, and the recall (also called sensitivity) indicates the percentage of the all-ground truth that was predicted correctly. As can be seen, the precision and recall finally converge to 0.94 and 1.00, respectively, which represents that the training of the neural network is completed.

The TM-SP in Fig. 10 is input to the neural network as a test set. Fig. 14 illustrates the classification result, in which the up-chirped LFM signal and the transient signal are successfully labeled. The value after the signal type indicates the confidence score. In summary, by introducing microwave photonics, the proposed system achieves the multidomain feature extraction and classification of the wideband and transient RF signals simultaneously.

IV. Conclusion

A photonics-based multidomain features extraction approach has been proposed and demonstrated. Through the TM-FT and the optical interference, the frequency and 2-D AOA of the RF signal are mapped to the time domain. Thus, the RF signal features in the time, frequency, and spatial domains can be extracted simultaneously without the complex digital computation. In the demonstrated experiments, the multidomain features extraction and classification for wideband RF signals and transient signals have been verified successfully. The proposed scheme can be applied for real-time features extraction and classification of RF signals in complex electromagnetic environments, such as cognitive radar, electronic reconnaissance, and radio astronomy observations.

References

[1] M. Amiri et al., "A second source of repeating fast radio bursts," *Nature*, vol. 566, no. 7743, pp. 235–238, Jan. 2019.

[2] D. Zhu and S. Pan, "Broadband cognitive radio enabled by photonics," *J. Lightw. Technol.*, vol. 38, no. 12, pp. 3076–3088, Jun. 2020.

[3] A. E. Spezio, "Electronic warfare systems," *IEEE Trans. Microw. Theory Techn.*, vol. 50, no. 3, pp. 633–644, Mar. 2002.

[4] P. Scanlon, I. O. Kennedy, and Y. Liu, "Feature extraction approaches to RF fingerprinting for device identification in femtocells," *Bell Labs Tech. J.*, vol. 15, no. 3, pp. 141–151, Dec. 2010.

[5] K. Gröchenig, *Foundations of Time-Frequency Analysis*. Berlin, Germany: Springer, 2001.

[6] D. Griffin and J. Lim, "Signal estimation from modified short-time Fourier transform," *IEEE Trans. Acoust., Speech, Signal Process.*, vol. ASSP-32, no. 2, pp. 236–243, Apr. 1984.

[7] H. M. Ozaktas and M. A. Kutay, "The fractional Fourier transform," in *Proc. Eur. Control Conf. (ECC)*, 2001, pp. 1477–1483.

[8] R. S. Pathak, *The Wavelet Transform*. Berlin, Germany: Springer, 2009.

[9] B. Friedlander, "A sensitivity analysis of the MUSIC algorithm," *IEEE Trans. Acoust., Speech, Signal Process.*, vol. 38, no. 10, pp. 1740–1751, Oct. 1990.

[10] U. Meye-Baese, "Fourier transforms," in *Digital Signal Processing With Field Programmable Gate Arrays*. Berlin, Germany: Springer, 2014, pp. 417–464.

[11] J. Yao, "Microwave photonics," *J. Lightw. Technol.*, vol. 27, no. 3, pp. 314–335, Feb. 1, 2009.

[12] X. Zou, B. Lu, W. Pan, L. Yan, A. Stöhr, and J. Yao, "Photonics for microwave measurements," *Laser Photon. Rev.*, vol. 10, no. 5, pp. 711–734, Jul. 2016.

[13] J. Capmany and D. Novak, "Microwave photonics combines two worlds," *Nature Photon.*, vol. 1, no. 6, pp. 319–330, Jun. 2007.

[14] T. Jannson, "Real-time Fourier transformation in dispersive optical fibers," *Opt. Lett.*, vol. 8, no. 4, pp. 232–234, 1983.

[15] T. A. Nguyen, E. H. W. Chan, and R. A. Minasian, "Instantaneous high-resolution multiple-frequency measurement system based on frequency-to-time mapping technique," *Opt. Lett.*, vol. 39, no. 8, pp. 2419–2422, 2014.

[16] A. Nuruzzaman, O. Boyraz, and B. Jalali, "Time-stretched short-time Fourier transform," *IEEE Trans. Instrum. Meas.*, vol. 55, no. 2, pp. 598–602, Apr. 2006.

[17] M. Li and J. Yao, "All-optical short-time Fourier transform based on a temporal pulse-shaping system incorporating an array of cascaded linearly chirped fiber Bragg gratings," *IEEE Photon. Technol. Lett.*, vol. 23, no. 20, pp. 1439–1441, Oct. 2011.

[18] M. Li and J. Yao, "Ultrafast all-optical wavelet transform based on temporal pulse shaping incorporating a 2-D array of cascaded linearly chirped fiber Bragg gratings," *IEEE Photon. Technol. Lett.*, vol. 24, no. 15, pp. 1319–1321, Aug. 2012.

[19] B. Zhang et al., "Impact of dispersion effects on temporal-convolution-based real-time Fourier transformation systems," *J. Lightw. Technol.*, vol. 38, no. 17, pp. 4664–4676, Sep. 2020.

[20] X. Xie, J. Li, F. Yin, K. Xu, and Y. Dai, "STFT based on bandwidth-scaled microwave photonics," *J. Lightw. Technol.*, vol. 39, no. 6, pp. 1680–1687, Mar. 2021.

[21] A. D. Gomes, H. Bartelt, and O. Frazão, "Optical Vernier effect: Recent advances and developments," *Laser Photon. Rev.*, vol. 15, no. 7, May 2021, Art. no. 2000588.

[22] C. Huang, X. Xie, K. Xu, and Y. Dai, "Optical computing STFT based on image depth learning," in *Proc. CLEO*, San Jose, CA, USA, May 2022, p. 122.

[23] C. Huang, X. Xie, K. Xu, and Y. Dai, "Dynamic intelligent measurement of multiple chirped signals of different types based on the optical computing STFT and the YOLOv3 neural network," *Opt. Lett.*, vol. 47, no. 18, pp. 4636–4639, 2022.

[24] S. R. Konatham et al., "Real-time gap-free dynamic waveform spectral analysis with nanosecond resolutions through analog signal processing," *Nature Commun.*, vol. 11, no. 1, p. 3309, Jul. 2020.

[25] J. Azaña, S. R. Konatham, R. Maram, and H. G. D. Chatellus, "Photonics-based real-time 2D (time-frequency) broadband signal analysis and processing," in *Proc. Int. Topical Meeting Microw. Photon. (MWP)*, Ottawa, ON, Canada, Oct. 2019, pp. 1–4.

[26] S. R. Konatham, H. G. de Chatellus, and J. Azaña, "Photonics-based real-time spectrogram analysis of broadband waveforms," *J. Lightw. Technol.*, vol. 38, no. 19, pp. 5356–5367, Oct. 2020.

[27] S. Reddy, R. Maram, and J. Azaña, "On-the-fly time mapped full spectrogram analysis of high-speed non-stationary microwave signals," in *Proc. Eur. Conf. Opt. Commun. (ECOC)*, Sep. 2018, pp. 1–3.

[28] M.-J. Wang, J.-L. Cai, F.-S. Tseng, and C.-Y. Hsu, "A low-complexity 2-D angle of arrival estimation in massive MIMO systems," in *Proc. Int. Comput. Symp. (ICS)*, Dec. 2016, pp. 710–713.

[29] J. Murakowski, G. J. Schneider, S. Shi, C. A. Schuetz, and C. W. Prather, "Photonic probing of radio waves for k-space tomography," *Opt. Exp.*, vol. 25, no. 14, pp. 15746–15759, 2017.

Authorized licensed use limited to: NANJING UNIVERSITY OF AERONAUTICS AND ASTRONAUTICS. Downloaded on October 18,2024 at 07:22:27 UTC from IEEE Xplore. Restrictions apply.

[30] J. C. Deroba, G. J. Schneider, C. A. Schuetz, and D. W. Prather, "Multifunction radio frequency photonic array with beam-space down-converting receiver," *IEEE Trans. Aerosp. Electron. Syst.*, vol. 54, no. 6, pp. 2746–2761, Dec. 2018.

[31] W. L. Beardell, C. J. Ryan, G. J. Schneider, J. Murakowski, and D. W. Prather, "Microwave photonic direction-finding spectrometer," *J. Lightw. Technol.*, vol. 41, no. 10, pp. 3057–3064, May 15, 2023.

[32] Y. Yang, C. Ma, F. Zhang, B. Fan, X. Wang, and S. Pan, "Photonics-based simultaneous angle of arrival and frequency measurement for multiple targets detection," in *Proc. Int. Topical Meeting Microw. Photon. (MWP)*, Matsue, Japan, Nov. 2020, pp. 14–17.

[33] Y. Yang et al., "Photonics-based simultaneous angle of arrival and frequency measurement system with multiple-target detection capability," *J. Lightw. Technol.*, vol. 39, no. 24, pp. 7656–7663, Dec. 2021.

[34] D. Zhu, W. Chen, and S. Pan, "Photonics-enabled balanced Hartley architecture for broadband image-reject microwave mixing," *Opt. Exp.*, vol. 26, no. 21, pp. 28022–28029, Oct. 2018.

[35] V. Durán et al., "Optical frequency combs generated by acousto-optic frequency-shifting loops," *IEEE Photon. Technol. Lett.*, vol. 31, no. 23, pp. 1878–1881, Dec. 1, 2019.

[36] S. Fernández-Menduiña, F. Krahmer, G. Leus, and A. Bhandari, "Computational array signal processing via modulo non-linearities," *IEEE Trans. Signal Process.*, vol. 70, pp. 2168–2179, 2022.

[37] C. J. Huang, H. Chen, and E. H. W. Chan, "Simple photonics-based system for Doppler frequency shift and angle of arrival measurement," *Opt. Exp.*, vol. 28, no. 9, pp. 14028–14037, Apr. 2020.

[38] R. J. Mailloux, *Phased Array Antenna Handbook*. Norwood, MA, USA: Artech House, 2017, pp. 63–99.

[39] J.-H. Kim, N. Kim, Y. W. Park, and C. S. Won, "Object detection and classification based on YOLO-V5 with improved maritime dataset," *J. Mar. Sci. Eng.*, vol. 10, no. 3, p. 377, Mar. 2022.

[40] Tektronix. *Fundamentals of Real-Time Spectrum Analysis*. Accessed: Jun. 15, 2015. [Online]. Available: https://download.tek.com/document/37W_17249_5_HR_Letter.pdf

Jiewen Ding (Student Member, IEEE) received the B.S. degree in electronic science and technology from the Nanjing University of Aeronautics and Astronautics, Nanjing, China, in 2019, where he is currently pursuing the Ph.D. degree.

His research interests include microwave photonic processing.

Dan Zhu (Member, IEEE) received the B.S. and Ph.D. degrees in electronic engineering from Tsinghua University, Beijing, China, in 2004 and 2009, respectively.

In May 2011, she joined the College of Electronic and Information Engineering, Nanjing University of Aeronautics and Astronautics, Nanjing, China, where she is currently a Professor. From May 2014 to May 2015, she was a Visiting Scholar with the Microwave Photonics Research Laboratory, University of Ottawa, Ottawa, ON, Canada. Her current research interests include microwave photonic signal processing and the system applications.

Prof. Zhu is a member of the IEEE Microwave Theory and Techniques Society, the IEEE Photonics Society, and the Optical Society of America.

Yue Yang (Student Member, IEEE) received the B.S. degree in electronic science and technology from the Nanjing University of Aeronautics and Astronautics, Nanjing, China, in 2018, where he is currently pursuing the Ph.D. degree.

His research interests include microwave photonic processing.

Zhouyang Pan (Student Member, IEEE) received the B.S. degree in electronic science and technology from the Nanjing University of Aeronautics and Astronautics, Nanjing, China, in 2021, where he is currently pursuing the Ph.D. degree.

His research interests include microwave photonic processing.

Shilong Pan (Fellow, IEEE) received the B.S. and Ph.D. degrees in electronic engineering from Tsinghua University, Beijing, China, in 2004 and 2008, respectively.

From 2008 to 2010, he was a "Vision 2010" Post-Doctoral Research Fellow with the Microwave Photonics Research Laboratory, University of Ottawa, Ottawa, ON, Canada. In 2010, he joined the College of Electronic and Information Engineering, Nanjing University of Aeronautics and Astronautics, Nanjing, China, where he is currently a Full Professor and the Executive Director of the Key Laboratory of Radar Imaging and Microwave Photonics, Ministry of Education. His research interests include microwave photonics, which includes optical generation and processing of microwave signals, analog photonic links, photonic microwave measurement, and integrated microwave photonics.

Prof. Pan is a Technical Committee Member of IEEE MTT-3 Microwave Photonics. He is a Fellow of OSA, SPIE, and IET. He was the Chair of a number of international conferences, symposia, and workshops, including the TPC Chair of the International Conference on Optical Communications and Networks in 2015 and the TPC Co-Chair of the IEEE International Topical Meeting on Microwave Photonics in 2017. He was selected as an IEEE Photonics Society Distinguished Lecturer in 2019. He is also an Associate Editor of *Electronics Letters* and a Topical Editor of *Chinese Optics Letters*.

Authorized licensed use limited to: NANJING UNIVERSITY OF AERONAUTICS AND ASTRONAUTICS. Downloaded on October 18,2024 at 07:22:27 UTC from IEEE Xplore. Restrictions apply.